Label-Free Imaging of Membrane Potential Using Membrane Electromotility

Seungeun Oh, Christopher Fang-Yen, Wonshik Choi, Zahid Yaqoob, Dan Fu, YongKeun Park, Ramachandra R. Dassari, and Michael S. Feld

G. R. Harrison Spectroscopy Laboratory, Massachusetts Institute of Technology, Cambridge, Massachusetts

Supporting Materials

Contents

Principle of quantitative phase imaging

The refractive property of live cells has been utilized in phase contrast microscopy and differential interference contrast microscopy as a means to create image contrast. On the other hand, a quantitative phase microscope measures the amount of optical phase delay produced by the cell's refractive index. Quantitative phase images provide an array of information about the cell including shape, dynamics, membrane mechanics, or mass (1-3).

In quantitative phase imaging, plane wave trans-illumination is often employed. The blue line above the cell in Figure S1a depicts the surface of constant phase of the illumination light. The refractive index determines the speed of light that propagates in a material. When the light pass through the cell, the speed of light is slower inside the cell than in the medium, hence, the wave front is delayed as depicted by the blue lines inside and below the cell in Fig. S1a. The magnitude of the phase shift introduced by the cell $\varphi(x,y)$ is expressed as the integral of the refractive index of the cell $n(x,y,z)$ along the axis of light propagation (z axis) where n_0 is the refractive index of the media and λ is the wavelength of the light in vacuum.

$$\varphi = \frac{2\pi}{\lambda}\int n(x,y,z) - n_0 dz \qquad \text{(Eq. 1)}$$

The refractive index distribution of a cell $n(x,y,z)$ is determined by the composition and the concentration of cellular materials. If the cell has a constant refractive index over the volume, the phase retardation $\varphi(x,y)$ is proportional to the thickness of the cell and the quantitative phase image can be used to infer the cell's height topography. (Fig. 2 F, J and G, L and Fig. S1)

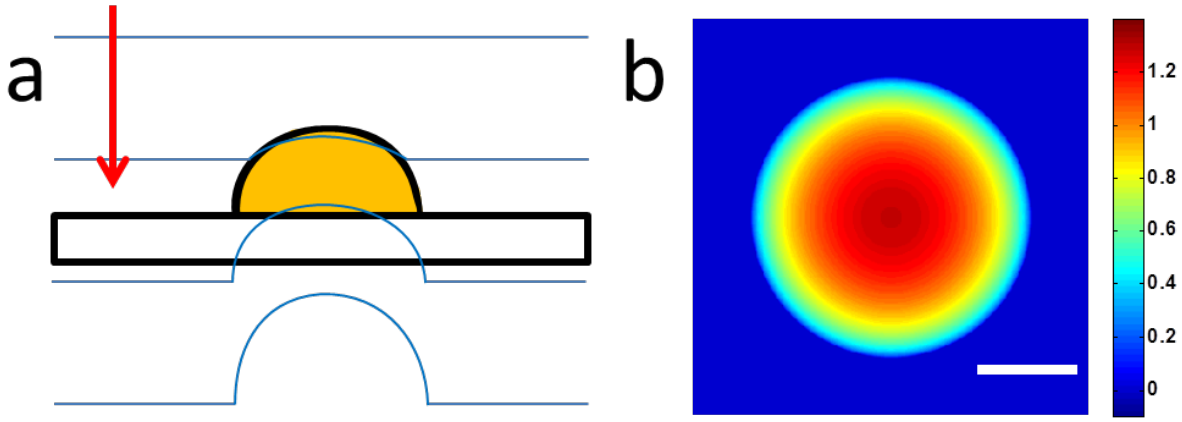

Figure S1. The wave front is retarded when it pass through a cell. (a) The wave front retardation introduced by a hemispherical cell of 10 μm diameter. The red arrow shows the axis of light propagation. (b) The simulated quantitative phase image of the hemispherical cell assuming the cell's refractive index 1.36 and medium's refractive index 1.336. The phase shift is proportional to the height of the cell. Color bar in radians. Scale bar 5 μm.

Interpretation of quantitative phase images

In general, the integral of refractive index measured in quantitative phase images can be altered by any changes in cell shape or material contents. One example is the gain and redistribution of cellular materials due to a live cell's growth and motility. Since these biological contributions are much slower than the time scale of the electrical stimulation used in this study we assume that any changes in the optical phase signal are due to physical changes in the cell as depicted in Fig. 2A. Among the three possible interpretations of the optical phase signals, we deduced that the fast intrinsic optical signals in HEK293 cells in this study are due to the redistribution of cellular materials by mechanical deformation. As shown in Figures 1F, 2H, and 2I and discussed in the text, the spatial distribution of the optical signal can be connected with

simple overall shape changes such as lateral displacement (Fig. 2H) or flattening (Fig. 2I). The models of deformation of the cell in Fig. 1 and Fig. 3 are illustrated in Fig. S2. A cell's adhesion to the substrate and organization of the cytoskeleton are likely to determine the overall geometry of cell deformation while the spatial variation of the cytoskeleton may give rise to the finer features in the optical phase signals.

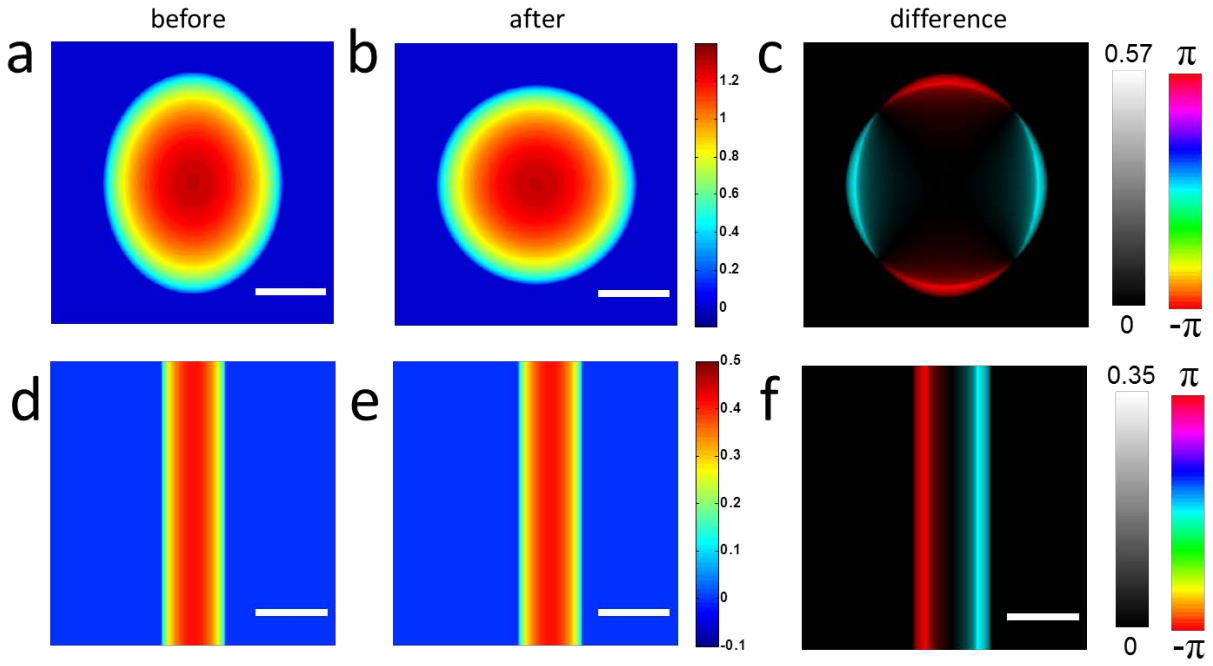

Figure S2. The schematic models that illustrate the relation between cell deformation and the optical phase signals of the cell in Figure 1 and the cell protrusion in Fig. 3. (a) An initially ellipsoidal shaped cell becomes more rounded (b) when the membrane tension increases with the change of transmembrane potential. (c) The difference of the quantitative phase images of (b) from (a) is shown in terms of amplitude and sign. The location of positive and negative signs resembles the optical phase signal in Fig. 1F. A tubular cell process (d) is laterally displaced by 1 μm (e). (f) The difference of the quantitative phase images of (e) from (d) is shown in terms of amplitude and sign. The location of positive and negative signs resembles the optical phase signal in Fig. 3B.

Lastly, the grains of the random color in the 'delay' image of Fig. 1E are caused by random background noise. The amplitude of the background fluctuation at a typical frequency was 0.17 mrad. Since the noise has no temporal correlation with the signal, its 'delay' (or the phase of the Fourier transform) is a random value between 0 and 2π (Fig. S3a). This causes an error in the delay measurement (Fig. S3b). When the signal is smaller than the size of the noise, the delay value is a random number between 0 and 2π as shown in Fig. S3c. This is the case in the background and the area of weak signal in Fig. 1E.

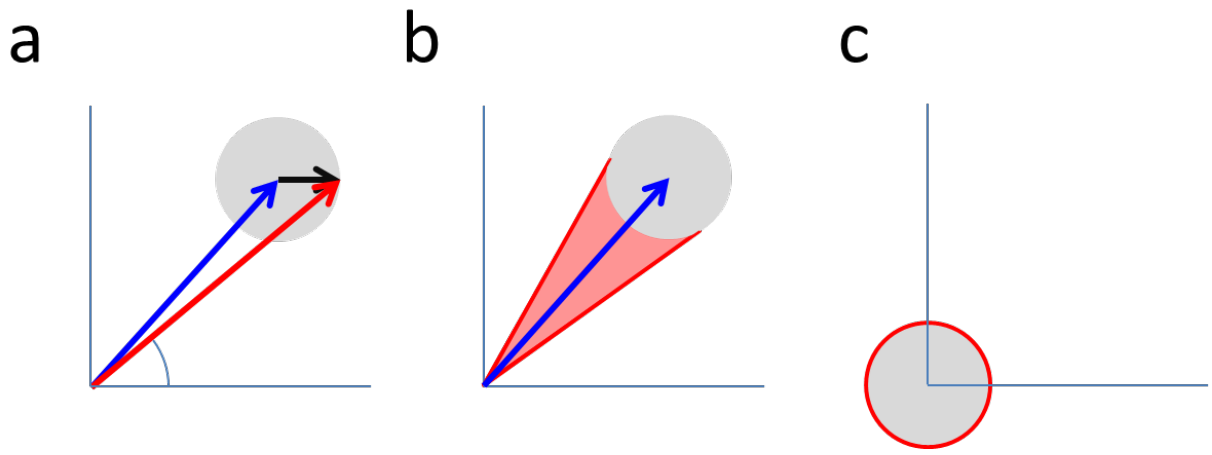

Figure S3. (a) The effect of the noise on the amplitude and delay of the optical phase signal is described by a vector sum. The cell deformation signal has length and phase (the angle of the vector) which are the amplitude and delay of the optical phase signal respectively. The noise (black vector) has random phase and may end anywhere within the gray disk. The radius of the gray disk is the mean amplitude of the noise. The observed signal (red vector) is the vector sum of the signal and the noise. (b) The phase of the observed signal deviates from the true signal phase by the addition of the noise. The red shaded area shows the range of observed phase. (c) When the signal is absent observed phase is a random angle between 0 and 2π.

Low-coherence diffraction phase microscope

We built a Low-coherence diffraction phase microscopy (LCDPM) by adapting Diffraction Phase Microscope (4) for the low coherence light source. The low coherence light source consists of a mode-locked Ti:Sapphire laser coupled to a single mode fiber. Its band width and coherence length are about 50 nm and 6 μm, respectively. A light from the laser was coupled into a single-mode fiber and an aspheric lens (L1) collimates the light coming out of the fiber. The beam diameter is 1mm when it reaches the sample. An inverted microscope (IX71, Olympus) consisting of the objective lens (L2, Olympus UPlanFLN, 40x 0.75NA) and the tube lens (L3) forms an image of the sample in the first image plane (IP1). The sample image is then relayed and magnified by two lenses (L4, L5, f=75mm and f=200mm respectively). A transmission grating (G, Edmund Optics high precision Ronchi ruling, 1000 lines per inch) is placed on the second image plane (IP2) to split the beam into multiple diffraction orders. Another set of lenses (L6, L7, f=150mm and f=250mm respectively) is arranged to relay the image to the camera at the third image plane (IP3). A pinhole and aperture (P) are placed in the Fourier plane (FP). The undiffracted light is filtered through the pinhole of P and becomes a plane wave after lens (L7) and serves as a reference field. The first order diffracted light goes through the aperture of P and contains the sample information. All other diffraction orders are blocked by P. To achieve the spatial resolution of the phase imaging to be diffraction-limited, the period of the grating is selected such that it is smaller than the diffraction-limited spot, 0.89 μm, at the sample plane. Interference images were recorded by a CMOS camera (Photron 1024PCI) positioned at the image plane (IP3), and later processed using the Hilbert transform as described in our previous report (4). The intensity image of interference pattern can be written as $I(x,y) = I_R + I_S + 2\sqrt{I_R I_S}\cos\left(\vec{k}_0 \cdot \vec{r} + \Delta\varphi(x,y)\right)$, where I_R and I_S are intensity of reference and

sample field, $\vec{k}_0$ is wave vector of grating image, and $\Delta\varphi(x,y)$ is the phase of sample field relative to reference field. A two-dimensional Fourier transform in x and y separates the interference pattern into three parts centered at DC, $+\vec{k}_0$, $-\vec{k}_0$, among which a disk around either $+\vec{k}_0$ or $-\vec{k}_0$ is selected and shifted to DC to be inverse Fourier transformed. The phase of the inverse Fourier transformed image is $\Delta\varphi(x,y)$.

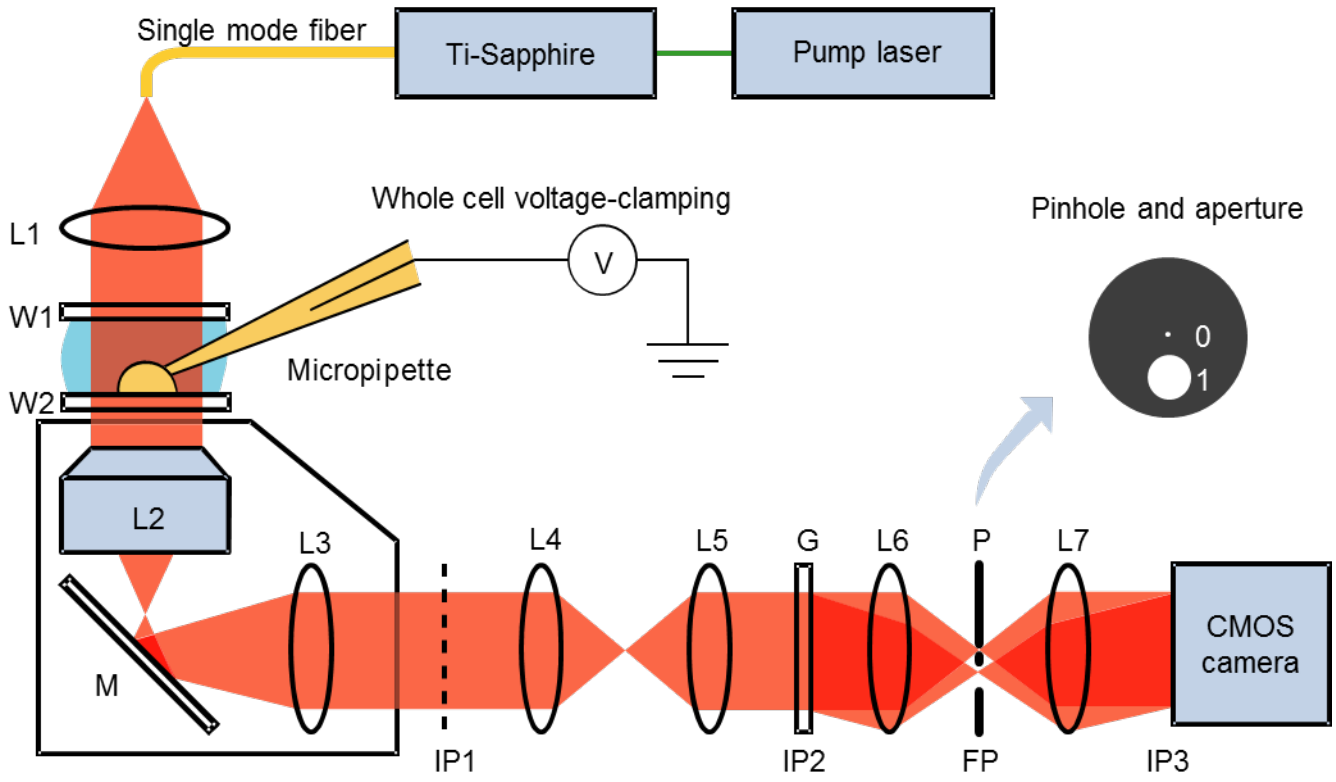

Figure S4. Schematics of the Low Coherence Diffraction Phase Microscope. L1-7: lenses, W1-2: cover glass, M: mirror, G: grating, P: pinhole and aperture, IP1-3: image planes, FP: Fourier plane.

Amplitude of optical signals

Since the optical phase signal has spatial variation within each cell, the signal amplitude can be quantified as (a) the peak amplitude or (b) the amplitude averaged over the area of the cell. The background noise can be also quantified in the same manner. Figure S5 shows the mean and the standard deviation of the signal amplitudes. The variations in the cell shape, cell stiffness and their adherence to the substrate are likely to underlie the cell to cell variation in signal amplitude.

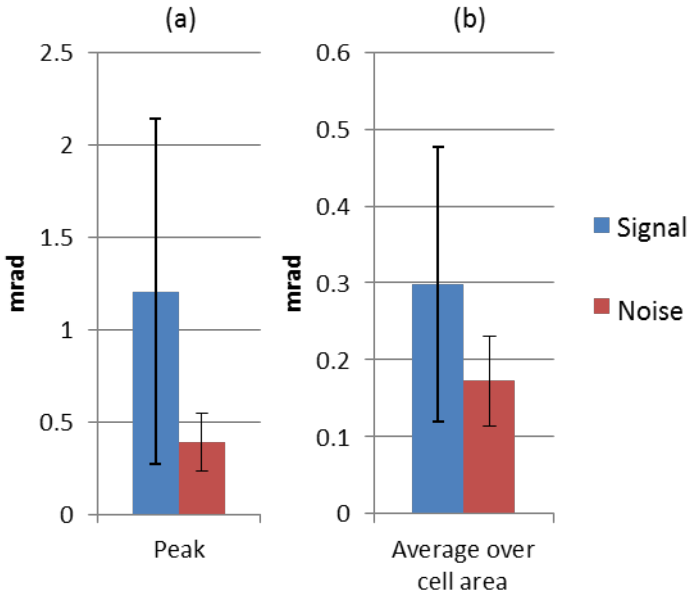

Figure S5. The population mean of optical phase signals from cells with intact patch clamping (blue) and the back ground noise in the absence of electrical stimulation (red). Error bar is the standard deviation. N=41. Peak signal amplitude was 1.2 mrad (SEM 0.15 mrad) and the average over the area of the cell body was 0.39 mrad (SEM 0.02 mrad). Peak noise amplitude was 0.34 mrad (SEM 0.02 mrad) and average noise amplitude was 0.17 mrad (SEM 0.01 mrad).

Electrical circuit of cells

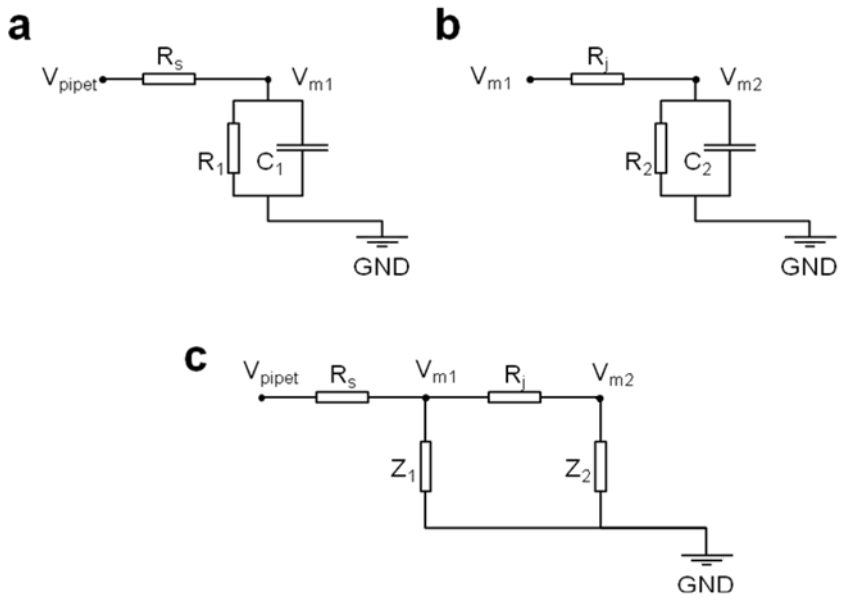

Figure S6. (a) Electrical circuit diagram of a patch clamped cell. (b) Electrical circuit diagram of a cell (cell2) electrically coupled to another cell (cell1) through gap junctions. (c) Cell1 is patch clamped and electrically coupled to cell2 through gap junction. V_{pipet} patch clamping pipette potential. V_{m1} membrane potential of cell1. V_{m2} membrane potential of cell2. R_1 membrane resistance of cell1. C_1 membrane capacitance of cell1. R_2 membrane resistance of cell2. C_2 membrane capacitance of cell2. R_s series resistance of patch clamping pipette. R_j junctional resistance of gap junction between cell1 and cell2. Z_1 impedance of cell1. Z_2 impedance of cell2. GND electrical ground.

Low-pass effect of patch clamping electrode

The micropipette for the patch clamping is pulled to have about 4 MΩ resistance in the bath solution, which is mostly determined by the size of the pipette tip. During the intracellular recording the resistance of the pipette is often higher (~10 MΩ) than the bath resistance. This is because cytoplasm is sucked into the pipette and clogs the tip. This resistance from the pipette tip is called the series resistance, R_S, as it is connected to the cell membrane resistance and capacitance in series. The membrane potential of the voltage clamped cell deviates from the pipette potential by the amount of voltage drop at the series resistance. Figure S6a shows an electrical circuit diagram of intracellular recording. Suppose the cell has membrane resistance R_1 and membrane capacitance C_1, its impedance at frequency f is $Z_1 = (1/R_1 + i2\pi f C_1)^{-1}$. The AC modulation of the membrane potential V_{m1} for a given AC modulation of the pipette potential V_{pipet} is determined by $V_{m1}/V_{pipet} = Z_1/(Z_1 + R_s) = [1 + R_S \times (R_1^{-1} + i2\pi f C_1)]^{-1}$. The absolute value of this ratio decreases with increasing frequency.

Electrical coupling through gap junction channels

Gap junction channels provide electrical conductance between two cells. The conductance of an individual channel is 50-140 pS and the total conductance between a pair of cells greatly varies depending on the number of channels (5,6). Suppose the membrane potential of pre-junctional cell (cell1) V_{m1} is modulated at frequency f. The change of the membrane potential of post-junctional cell (cell2) V_{m2} can be calculated based on Figure S6b. The post-juctional potential is smaller than the pre-junctional potential by the voltage drop at the junctional resistance.

Therefore, $V_{m2}/V_{m1} = Z_2/(Z_2 + R_j) = [1 + R_j \times (R_2^{-1} + i2\pi f C_2)]^{-1}$, where R_j is the gap junction resistance between cell1 and cell2, R_2 is the membrane resistance, C_2 the membrane capacitance, and Z_2 the impedance of cell2. Fig. 3D shows that the membrane potential modulations are similar in the size among the 'cell 1' and other neighboring cells in the normal condition, indicating very small electrical resistance of the gap junctions. On the other hand, CBX makes the membrane potential modulation rapidly attenuated as it propagates to the distant cells, showing an increase in gap junction resistance. (Fig. 3E)

Suppose that cell1 is patch clamped and that cell1 is electrically coupled to cell2 through gap junction channels. As in Fig. S6c, the electrical load attached to the patch clamping pipette is the combined circuit of cell1 and cell2. Since cell1 and cell2 are connected in parallel, the effective impedance of the combined circuit, Z_{cells}, has lower resistance and higher capacitance than the individual impedance Z_1 and $R_j + Z_2$. Therefore, if many cells are strongly coupled (small R_j) to cell1, the effective impedance of the gap junction coupled cells Z_{cells} can be much smaller than that of any isolated cell. In such case, the voltage clamping of the membrane potential is significantly smaller than the pipette potential as $V_{m1}/V_{pipet} = Z_{cells}/(Z_{cells} + R_s)$ becomes small. The increase of 'cell 1' signal in the CBX condition is explained likewise. When CBX reduces the electrical conductance of gap junctions, the resistance of the electrical circuit as a whole increases. Since the voltage drop at the series resistance increases with the proportion of the series resistance to the total resistance, higher total resistance results in smaller voltage drop at the series resistance and larger membrane potential modulation delivered to the cell.

Supporting References

1. Shaked, N. T., J. D. Finan, F. Guilak, and A. Wax. 2010. Quantitative phase microscopy of articular chondrocyte dynamics by wide-field digital interferometry. J Biomed Opt 15:010505.

2. Park, Y., C. A. Best-Popescu, R. R. Dasari, and G. Popescu. 2011. Light scattering of human red blood cells during metabolic remodeling of the membrane. J Biomed Opt 16:011013.

3. Popescu, G., Y. Park, N. Lue, C. Best-Popescu, L. Deflores, R. R. Dasari, M. S. Feld, and K. Badizadegan. 2008. Optical imaging of cell mass and growth dynamics. Am J Physiol Cell Physiol 295:C538-544.

4. Ikeda, T., G. Popescu, R. R. Dasari, and M. S. Feld. 2005. Hilbert phase microscopy for investigating fast dynamics in transparent systems. Opt. Lett. 30:1165-1167.

5. McMahon, D. G., A. G. Knapp, and J. E. Dowling. 1989. HORIZONTAL CELL GAP-JUNCTIONS - SINGLE-CHANNEL CONDUCTANCE AND MODULATION BY DOPAMINE. Proc. Natl. Acad. Sci. U. S. A. 86:7639-7643.

6. Young, J. D. E., Z. A. Cohn, and N. B. Gilula. 1987. FUNCTIONAL ASSEMBLY OF GAP JUNCTION CONDUCTANCE IN LIPID BILAYERS - DEMONSTRATION THAT THE MAJOR 27-KD PROTEIN FORMS THE JUNCTIONAL CHANNEL. Cell 48:733-743.